Kwiatek, G., Bohnhoff, M., Dresen, G., Schulze, A., Schulte, T., Zimmermann, G., Huenges, E. (2010): Microseismicity induced during fluid-injection: A case study from the geothermal site at Groß Schönebeck, North German Basin. - Acta Geophysica, 58, 6, 995-1020

DOI: 10.2478/s11600-010-0032-7

Microseismicity induced during fluid-injection: A case study from the geothermal site at Groß Schönebeck, North German Basin

Authors:

Grzegorz Kwiatek[a], Marco Bohnhoff[a], Georg Dresen[a], Ali Schulze[a], Thomas Schulte[a], Günter Zimmermann[a], Ernst Huenges[a]

[a] Helmholtz Centre Potsdam, GFZ German Research Centre for Geosciences, Telegrafenberg, D14473 Potsdam, Germany

Corresponding author: Grzegorz Kwiatek, e-mail: kwiatek@gfz-potsdam.de, Tel. +49 331 288 1384, Fax: +49 331 288 1328

Abstract

The technical feasibility of geothermal power production in a low enthalpy environment will be investigated in the geothermal site at Groß Schönebeck, North German Basin, where a borehole doublet was completed in 2007. In order to complete the Enhanced Geothermal System, three massive hydraulic stimulations were performed. To monitor injection-induced seismicity during fluid injection a seismic network was deployed including a single 3-component downhole seismic sensor at only 500 m distance to the injection point. Injection rates reached up to 9 m^3/min and maximum injection well-head pressure was as high as ~60 MPa.

A total of 80 very small ($-1.8 < M_W < -1.0$) induced seismic events were detected only at the deep borehole sensor. The hypocenters were determined for 29 events using P and S wave onset times and polarization analysis. The events show a strong spatial and temporal clustering and a maximum seismicity rate of 22 events per day. Spectral parameters were

estimated from the downhole seismometer and related to those from other types of induced seismicity. The majority of events occurred towards the end of stimulation phases indicating a similar behavior as observed at similar treatments in crystalline environments but in our case at smaller level of seismic activity and at lower magnitudes.

Keywords:

induced seismicity, spectral analysis, hydraulic stimulation, enhanced geothermal systems

1. Introduction

Passive seismic monitoring (PSM) of microseismicity induced during hydraulic fracturing through massive fluid-injection is a well-established method to map the fracture growth, reservoir extent and permeability enhancements in hydrocarbon or geothermal reservoirs. Systematic fluid-injection was pioneered at the Rangely Oil Field, Colorado confirming the hypothesis that earthquakes may be triggered by increase of fluid pressure (Raleigh et al., 1972). Since the Rangely experiment, many of PSM campaigns have been pursued in the petroleum industry confirming the direct correlation between injection flow rate and pressure and rate of induced seismicity (e.g. Kovach, 1974; Albright and Pearson, 1982; McGarr, 1991; Zoback & Harjes, 1997; Phillips et al., 1998; 2002). On the other hand, Tosha et al. (1998) studied the seismicity recorded at Kakkonda Geothermal Field in Japan and found no clear relationship between the well operations and microearthquake swarms during the injections. However, when production was shut down, swarm activity occurred in the nearby area. They attributed this to a change in the characteristics of the geothermal reservoir due to multiple injections. The changes in spatial and temporal distribution of seismic events were also reported by Nagano et al. (1994) who pointed out, that the seismicity did not occur in previously stimulated zones (the so-called Kaiser effect, also reported in e.g. Baisch et al.,

46 2002). The changes in seismic event rate during multiple injections were also reported by
47 Simiyu (1999) who noted the time lag between consecutive stimulations in the same reservoir.
48 All these observations led to the development of downhole seismic recording during reservoir
49 stimulation as a key method to monitor the migration of the injected fluid at depth and thus
50 develop quantitative models of the reservoirs.

51 In recent years, there has been a considerable improvement in seismic data acquisition:
52 e.g. using of sensitive sensors with high sampling rate, installation of extensive seismic
53 networks composed both of surface and borehole seismometers, located close to injection
54 areas (e.g. Evans et al., 2005; Bourouis & Bernard, 2007). It enables recording of high-quality
55 seismograms of very small events and allows for more sophisticated analysis schemes of
56 small-scale brittle failure processes related to hydraulic stimulation. It improved primarily the
57 precision of standard source parameter determination such as hypocenter location and event
58 magnitude. It also allowed for calculation of other source parameters such as fault plane
59 solutions, seismic moment tensors, moment magnitudes, source sizes as well as stress drop
60 estimates.

61 Zoback & Harjes (1997) analyzed almost 400 microearthquakes ($M<1.2$) induced by
62 injection of 200 m^3 of heavy brine at almost 9 km depth at the KTB deep drill hole in
63 Germany in 1994. They reported microearthquakes grouped spatially into clusters that were
64 induced by very small pore pressure perturbations. The highly similar waveforms suggested
65 successive movement of adjacent fault patches. Jost et al. (1998) used the same waveform
66 dataset to calculate compound fault plane solutions and invert the waveforms for the relative
67 source time function and calculate the rupture directivity using the empirical Green's function
68 technique (Hartzell, 1978, Mueller, 1985). They also performed the relative moment tensor
69 inversion. They found pure double-couple events supporting the results previously obtained

by Zoback & Harjes (1997). They also found that the static stress drop is increasing with seismic moment. In a similar experiment at the same site six years later (Baisch et al., 2002; Bohnhoff et al., 2004) the seismic network detected 2799 events ($-1.2 < M_L < 1.1$). 237 events had a sufficient signal-to-noise ratio at the surface stations to determine reliable hypocenters. A strong spatiotemporal clustering was observed with clouds of seismicity moving away from the borehole with time. 125 focal mechanisms were calculated and used in the following stress tensor inversion. The study confirmed the strike-slip regime observed at KTB. Shapiro et al. (2006) showed that only positive pore pressure perturbations induced seismicity and they confirmed that fluid pressure diffusion is a dominant mechanism of seismicity triggered by fluid injections in KTB. Kümpel et al., (2006) analyzed the seismicity related to injection test performed at KTB in 2004-2005. They found that the seismicity was much weaker than in previous experiments. They attributed it to the lower pressure build-up and increased transmissivity of the fault system. Jahr et al. (2008) investigated the deformation caused by water injected in KTB. They found the maximum deformation of ~3 cm correlated with the region of the observed induced seismicity.

Extensive downhole seismic monitoring of induced seismicity was also performed at the European Deep Geothermal Energy Program site in Soultz-sous-Forêts, France. The sequence of fluid injection/production experiments was performed in 1993, 2000 and 2003-2005 (see Evans et al., 2005; Cuenot et al., 2006; Darnet et al., 2006; Charléty et al., 2007; for a comprehensive review). The maximum flow rate was reached in 2003 with 5.4 m^3/min when a total of 37000 m^3 of water was injected. High seismicity rate was observed almost instantaneously with the start of injection, except when the target area had been stimulated during previous injections (Charléty et al., 2007). In general, occurrence rates of events were sensitive to changes in the flow rate and the microseismic activity decayed exponentially after

94 shut-in of the boreholes. The stronger microearthquakes occurred just after the shut-in phase.
95 Charléty et al. (2007) also observed a slight increase in average magnitude values during shut-
96 in in comparison with injection periods and a slow decrease in the number of earthquakes
97 from one year to another. Various spatial structures of seismicity were observed including
98 planes with sizes much smaller than the source dimension of the individual events suggesting
99 a multiple breakdown of the asperities. Hundreds of double-couple fault plane solutions were
100 calculated (Cuenot et al., 2006; Charléty et al., 2007) indicating a normal faulting
101 environment in the proximity of injection wells with strike-slip components at greater
102 distances. Indications for non-double-couple seismic events were observed and considered to
103 be related neither to numerical artifacts, nor to possible curvature of the faults (i.e. complex
104 source processes) nor to the opening and shearing mode of failure (Cuenot et al., 2006). They
105 were attributed to either cooling around the injection or large increase in overpressure. No
106 evidence for tensile faulting was observed (Charléty et al., 2007). No clear evidence was
107 found for the breakdown in self-similarity of seismic events (i.e. moment dependent stress
108 drop).

109 In this study we analyze microseismicity induced during a massive (injection rate
110 reaching $9m^3$/min) fluid injection experiment performed at the geothermal site in Groß
111 Schönebeck, Germany, in August 2007. Seismic monitoring was achieved by a seismic
112 network including a borehole geophone as close as 500 m to the injection point. We
113 investigate the spatial and temporal distribution of the events to monitor the propagation of
114 the injection. We determine the source characteristics such as seismic moments and source
115 radii in order to assess the earthquakes' strength and extent of ruptured faults. We investigate
116 whether there are any signatures of the type of event (shear/extensional failure) by comparing
117 the energy radiated from P and S waves. We try to assess the damaging potential of recorded

seismicity by comparing the seismic moment and radiated energy.

2. Site description

The Groß Schönebeck Research wells E GrSk 3/90 (here abbreviated as EG) and Gt GrSk 4/05 (GG) are located in the eastern part of the North German Basin, which is characterized by sedimentary deposits of several km thickness and absence of recent tectonic activity. Low enthalpy geothermal reservoir rocks (see Zimmermann et al., 2009a, Zimmermann and Reinicke, 2010, for details) are to be found here as siliciclastic sediments and volcanics of the lower Permian at an average depth of about 4000 m and at formation temperatures of up to 150°C. The existing well EG was used for repeated stimulation treatments to investigate scenarios of enhancing productivity of thermal fluid recovery from the underground (Zimmermann et al. 2009b). Subsequently the doublet has been completed with a second well GG with a total depth of 4400 m. In order to maximize the zone, over which the subsurface heat exchanger can be created, this new well is inclined with 47° in the reservoir section. It was drilled in the direction of the minimum horizontal stress σ_h=288° (Moeck et al., 2007) for optimum hydraulic fracture alignment. Hence the orientation of any hydraulically induced fractures is expected to be 18°N, i.e. in the direction of the maximum horizontal stress. While the deep well GG was used to perform fluid injection to locally enhance permeability and thus fluid circulation between both wells, a downhole seismic sensor was deployed in well EG at 3800 m depth. The sensor is located at only 500 m distance to the injection point providing the opportunity to monitor induced seismicity as low as M_W~-2.0.

3. Injection experiment

Three hydraulic treatments were performed in well GG in summer 2007: One in the Lower

Rotliegend volcanic section and two in the sandstone section of the Upper Rotliegend Dethlingen formation (see Figure 1). The entire well was cased and cemented except for the lowermost 40 m, where an uncemented perforated casing was installed over an open hole section. The permeable volcanic rocks were stimulated through a massive cyclic waterfrac treatment (Zimmermann et al., 2008). A cyclic injection procedure was chosen following technical constraints such as availability of fresh water and the expectation, that a cyclic, high flow rate injection (up to 9 m^3/min) will enhance fracture propagation and performance compared to a constant and low (3 m^3/min) stimulation. The first and major injection was performed over a period of 6 days, between August 9th and August 14th, 2007. A total amount of 13,000 m³ of water was injected. The maximum injection well-head pressure reached 58.6 MPa. Two other treatments were carried out in the porous and permeable Upper Rotliegend sandstone formations over the intervals of 4122 m to 4118 m and 4204 m to 4208 m, respectively. 500 m³ of crosslinked gel were injected in each of the treatments (Zimmermann et al., 2009a, Zimmermann and Reinicke, 2010), at maximum well-head pressures of 49.5 MPa and 38.0 MPa, respectively. In the following analysis we primarily focus on the major injection in volcanic rocks.

4. Seismic network

The site conditions for a near-surface based seismic network are unfavorable due to the thick sedimentary formations and evaporite sequences at depth. Both result in low signal to noise ratios of seismic waves decreasing with distance from the source (see Weber et al., 2005). Nevertheless, we deployed a seismic network consisting of seven three-component seismometers including one downhole seismometer operated at 3800 m depth in EG well at only ~500 m distance to the injection point (see Figure 2). The additional six instruments were installed both at the surface and in shallow (~60 m deep) boreholes, at about 3 km

165 distance from the well head. The deep borehole sensor was of type GEOSPACE HS-1 with
166 natural frequency 15 Hz and sampling rate 1000 Hz. The sensors located at the surface and in
167 shallow boreholes were equipped with MARK SERCEL L4-3C seismometer (1 Hz) and
168 SENSOR SM6-B geophones (4.5 Hz), respectively, and all sampled at a rate of 200 Hz. The
169 acquisition system was continuously recording between 2nd and 22nd August 2007 framing the
170 injections into the volcanic and sandstone layers. Data recovery rate of the network was 95%.
171 We used regional seismic events from the Legnicko-Glogowski Copper District in Poland to
172 calibrate the network (8th August 2007, M_L=3.7, and 15th August 2007, M_L=4.3, R=~230 km
173 according to SZGRF network). Those recordings and a calibration shot fired at 4000 m depth
174 in the injection well (about ~500 m from the deep borehole sensor) see Figure 3), close to the
175 perforation point, were used to determine the orientation of the deep downhole sensor with an
176 uncertainty of 15°. Unfortunately, the calibration shot could not be used to estimate the P and
177 S wave velocities, as its origin time was not synchronized to acquisition system clock due to
178 technical problems.

179 Noise levels at the seismic sensors were sufficiently low prior to injection and during
180 relatively low injection rates (not exceeding 2 m^3/min). However, during high injection rates,
181 the deep downhole sensor was seriously contaminated by noise generated by the water pumps
182 extending almost over the entire frequency range of the recorded seismic energy (Figure 4).
183 As a result, the recording and detection conditions were significantly limited during the
184 periods of larger injection rates.

185 5. Induced Seismicity

186 A total number of only 80 microearthquakes were detected by the downhole seismometer
187 using a LTA/STA (long-term average/short-term average) detection algorithm supported by

188 an autoregressive AIC picker (Yokota et al., 1981; Leonard & Kennett, 1999) to increase the
189 detection accuracy. The P and S onsets were measured with uncertainty not exceeding
190 3 samples (i.e. 3 ms). The estimated magnitudes of induced microseismic events were
191 unexpectedly low and ranged $-1.8 < M_W < -1.0$. In consequence, because of source-receiver
192 distances exceeding 5 km, high frequency content of the recorded seismic events (>200 Hz)
193 and attenuation of seismic signals, the events were only recorded by the three-component
194 deep borehole sensor and were too small to be detected by the surface stations. Therefore, the
195 entire analysis had to be focused on recordings from the one three-component deep borehole
196 sensor. The analysis using one sensor limited the reliability of obtained source parameters;
197 nevertheless, we decided to calculate the source parameters in order to get an insight in
198 seismicity induced by the stimulation.

199 Only a few seismic events were recorded before the first injection test that started on
200 9th of August. During the stimulation test (Aug 9-10th), the injection rate varied between 0 and
201 5 m^3/min whereas the well-head pressure ranged between 0 and 50 MPa (Figure 5).
202 A relatively large number (20) of seismic events occurred almost instantaneously (~20 min)
203 during the injection test (Figure 5, sequence A). For some of the events, the S-P times could
204 be determined and we were able to estimate at least the hypocentral distance. The majority of
205 S-P times did not exceed 0.1 s. Assuming median P-wave (V_P = 4388±450 m/s) and S-wave
206 velocities (V_S = 2575±250 m/s) as determined from 3 core sample measurements of
207 sandstones (Trautwein & Huenges, 2005) , it corresponds to hypocentral distances smaller
208 than 600 m. The hypocentral distances coincide with the distance between the deep sensor
209 location and injection area. Since we do not have information on the incident angle of the
210 recorded seismicity we speculate, that the events from sequence A occurred in sandstones, in
211 the direct proximity of injection point.

No significant increase in seismic event rate was observed after the start of the longer injection phase on August 11 contradicting earlier findings during comparable experiments. This lack of seismicity may be only partially explained by the increase in pumping noise level (on 11th of August the injection rate reached two times its peak value i.e. 9.38 m^3/min) as there were also a few episodes with much lower injection rate (and thus lower noise level) where almost no seismicity was detected. On 13th of August, about two hours after the flow rate dropped from 5 m^3/min to less than 1 m^3/min (decrease in well-head pressure from 50 to 30 MPa), the most prominent seismic sequence occurred (sequence B in Figure 5). The sequence lasted about 1.5 hours and consisted of more than 20 events with clear S wave onsets whereas P-wave onsets were difficult to be identified in some cases. Interestingly, six events of this sequence formed three pairs in time with ~200, ~600 and ~700 ms difference between P-wave onsets, respectively. The S-P time appeared to be consistent for all events (110-120 ms, 683-751 m). The hypocenter determination performed with the three-component deep borehole sensor, described in the following section, confirms the common spatial origin of these events as shown in Figure 6. The cross-correlation analysis of cluster B events also reveals similarity of waveforms (Figure 7) with correlation coefficients ranging between 0.61 and 0.84.

The last sequence (C) occurred after the end of injection on 14th of August. This sequence contains 12 events (9 located) with high signal-to-noise ratio for both P and S arrivals. The first events from sequence C occurred 20 minutes after the total shut-in of the well. Sequence C could be divided into two subgroups. The first subgroup (C1) consisted of six events with waveforms similar to that from cluster B (cross-correlation coefficients 0.65-0.95, 0.8-0.98 within C1 cluster). The almost identical S-P times of 113-115 ms, azimuths and incidence angles correspond to the same parameters estimated for cluster B (cf. Figures 5 and

236 6). The second subgroup (C2) comprises at least three events (cross-correlation coefficients
237 0.61-0.71) with different waveforms and azimuths. S-P times range from 86 to 93 ms. Three
238 examples of recorded seismic events from groups B, C1 and C2 are shown in Figure 7. The
239 detailed information on seismic parameters is listed in Table 1.

240 After shut-in, the number of recorded seismic events dropped to a few events per day
241 (only two could be located) while the well remained unchanged for four days until the next
242 experiment was performed on August 18^{th} / 19^{th}. The injection into a more porous and
243 permeable sandstone formation induced only two very weak events, hardly recorded by the
244 deep borehole sensor (additional two preceded the injection).

245 6. Hypocenter Determination

246 In the first step, we estimated the spatial distribution of the recorded seismicity using the 3
247 component borehole sensor. The hypocentral distances ranged between 680 and 750 m and
248 between 536 and 580 m for clusters B/C1 and C2, respectively. The picking accuracy for P
249 and S onsets for the noisiest events analyzed does not exceed three samples (corresponding to
250 the maximum difference ±19 m in hypocentral distance). Its contribution to the overall error
251 in hypocentral distance is thus smaller than the one resulting from uncertainties in the velocity
252 model used, which is are of order ±70 m (the estimations based on ±10% variation of P and S
253 velocity of core samples measured). We assumed overall uncertainty (3σ) of distance
254 estimation to be ±89 m. To determine the direction of incoming waves at the downhole sensor
255 we applied a polarization analysis (e.g. Plesĭnger et al., 1986). In addition, the results were
256 tested by a manual rotation of the waveforms towards the maximum polarization of the P
257 wave. Assuming isotropic medium and straight seismic ray paths between seismic source and
258 seismometer, a total number of 29 events could be located using S-P times as a measure of

distance (Figure 6). We compared results from automatic and manual polarization analysis and concluded, that the uncertainty for the azimuth angle and angles of incidence is ±10º and ±5º, respectively. This corresponds to maximum horizontal and vertical errors of ±125 m and ±63 m for clusters B and C1, respectively. Accordingly, the location uncertainties for cluster C2 are ±97 m and ±49 m, respectively. The spatial distribution of seismic events from cluster B and C1 and mutual similarity of their waveforms suggests that all events occurred on the same (fault) plane and that they might reflect earthquakes that repeatedly re-ruptured the same fault patch, as noted by e.g. Baisch and Harjes (2003). We fitted location coordinates, using least-squares technique to the plane surface. The strike and dip of the resulting plane (marked in Figure 6) were found to be 17º and 52º, respectively, which is in good agreement with the stress regime in the studied area (see e.g. Moeck et al., 2008). We found events from clusters B and C1 moving outwards from the injection area with progressing time (i.e. the shallower events occurred in the later stages of injection, see Figure 6). This possibly reflects the migration of fluids through volcanic rocks and sandstones.

7. Assessment of source parameters

We made an attempt to assess the source parameters using the borehole sensor to gain some insight into the seismic moment release caused by injection. We also wanted to achieve a rough estimation of the fault sizes' and the damaging potential of seismic events induced by the injection.

The preprocessing started with rotation of 3-component waveform data into a local ray coordinate system (Radial, SV and SH) of the maximum P wave polarization. Then, the ground velocity records were integrated to obtain the displacement waveforms. Selected parts of P- and S-phases (typically not longer than 80-90 ms) were tapered using a 10% von Hann’s

window. A Fast Fourier Transformation (FFT) was then applied to both the ground velocity and displacement waveforms. The resulting spectra were multiplied by a factor of $\exp\left(\frac{\pi f R}{V_C Q_C}\right)$, where R is the distance and V_C is the P or S wave velocity, to correct for frequency-independent attenuation. We assumed Q_P=300 and Q_S=150 (these values seemed to produce the best fit between obtained spectra and Ω^{-2} source model). As the exact values of the attenuation factor are in fact not known in the direct vicinity of the borehole and injection area, we examined the influence of applied Q correction on calculated source parameters. We assumed quality factor may vary in a range 200-400 and 100-200 for P and S wave, respectively, and then estimated the uncertainty of derived source parameters by the rule of uncertainty propagation. The attenuation correction had no visible effect on spectral level (therefore, e.g., seismic moment) but it strongly affected the estimation of energy flux and corner frequency. An example of amplitude spectrum is shown in Figure 8.

The spectral parameters were estimated from horizontal components for events from clusters B and C, assuming Ω^{-2} Brune's model (Brune 1970, 1971) and the methodology developed by Andrews (1986). The bandwidth used in this study ranged from 50 Hz to 300 Hz. The reliable estimation of source parameters from radial component was possible only for cluster C (no noise from water pumps) and selected events from cluster B. Source parameters were corrected for the limited frequency band considered, according to Di Bona and Rovelli (1988) and Ide and Beroza (2001). The seismic moment was calculated using:

$$M_0 = \frac{4\pi\rho V_C^3 R}{R_C}\Omega_C, \qquad (1)$$

where ρ = 2900 kg/m^3 is the medium density, V_C is either P or S wave velocity, R is the

source-receiver distance calculated from the S-P propagation time difference and Ω is the spectral level investigated manually on seismograms (for S waves, $\Omega_S = (\Omega_{SV}^2 + \Omega_{SH}^2)^{0.5}$). The additional term R_C is the correction accounting for radiation pattern. In this study, we used Monte-Carlo methodology provided in Boore & Boatwright (1984) to calculate R_C. We assumed that the most probable focal mechanism ranges from normal to strike slip faulting (rake from -90º to 0º), as suggested by Moeck et al. (2009). We assumed fault strike equal to 17º±15º and dip equal to 52º±5º. We found R_P and R_S ranged 0.35-0.49 and 0.86-0.90, respectively. We used median values of R_P=0.42±0.07 and R_S=0.88±0.02 to correct for radiation pattern. The corrections for a free surface effect and site were not applied due to the downhole location of the sensor (e.g. Gibowicz & Kijko, 1994). We assumed that the seismic moment may be biased by a factor of 2 due to manual picking. The moment magnitude was computed using the standard relationship (Hanks & Kanamori, 1979): $M_W = 0.66 \log M_0 - 6.07$. The overall uncertainty of M_W estimation, affected primarily by the uncertainty of the picking process and velocity model, did not exceed ±0.30.

The radiated energy for either P or S wave is calculated following Boatwright and Fletcher (1984):

$$E_C = 4\pi\rho V_C \langle R_C \rangle^2 \left(\frac{R}{R_C} \right)^2 J_C , \qquad (2)$$

where $J_C = 2\int |V(f)|^2 df$ is the measure of the seismic energy flux (Snoke, 1987) and *V(f)* is the ground velocity FFT spectrum of either P or S phase, corrected for attenuation. The average radiation coefficient equaled $<R_P>$=0.52 and $<R_S>$=0.63 (Boore and Boatwright, 1984). The radiated energy was corrected for the limited frequency band according to Ide and Beroza (2001). The P and S energy could only be calculated for events from cluster C. The

main source of uncertainties (98% of total uncertainty) originates from assumed variations in the quality factor and the energy flux can vary by a factor 0.66-2.52 and 0.61-3.00 for P and S wave, respectively. However, persistent pumping noise and high-pass filtering of signals make the quantification of radiated energy difficult and the error may be even higher.

The corner frequency f_C was investigated manually on-screen and then averaged over P and S waves. Similarly to radiated energy, the estimations of corner frequency suffered from assumed variations in the quality factor. The calculated values may be biased by a factor of 0.87-1.36 and 0.84-1.43 for P and S wave, respectively.

The remaining source parameters assessed in this study were calculated as follows:

$$r = \frac{K_C V_S}{2\pi f_C}, \tag{4}$$

$$\sigma_a = \mu \frac{E}{M_0}, \tag{5}$$

$$\Delta\sigma = \frac{7}{16}\left(\frac{M_0}{r^3}\right), \tag{6}$$

where r is the source radius, σ_a is apparent stress and $\Delta\sigma$ is the stress drop (e.g. Snoke, 1987). K_C is the constant depending on the wave type and the source model used. We used the quasidynamic circular fault model of Madariaga (1976) to calculate the fault size and assumed that K_P=2.01 and K_S=1.32, appropriate values when focal mechanisms are not known. These correction coefficients provide a reasonable source size in case of small and induced seismic events (Gibowicz & Kijko, 1994). For the apparent stress we assumed the rigidity coefficient μ equal to ρVs^2. Source parameters for 29 events with $-1.8 < M_W < -1.0$ are presented in

344 Table 1.

345 Figure 9a presents the relationship between radiated energy E_S and E_P calculated from
346 P and S phases for clusters C1 and C2. A similar relationship for seismic moments is shown
347 in Figure 9b. For cluster C1, the E_S/E_P ratio ranges from 21.9 to 34.9 (mean value 27.0). The
348 obtained values for cluster C1 are in agreement with other studies, where the energy radiated
349 in P waves commonly tends to be a small fraction (0.05-0.3) of that radiated in S waves
350 (Boatwright and Fletcher, 1984). The values of the E_S/E_P ratio for cluster C2 are lower and
351 ranges 1.87-17.31. However, the magnitudes are small and the signal-to-noise ratio is rather
352 poor and we cannot draw any conclusions. The ratio of ${M_0}^S/{M_0}^P$ ranges from 0.47 to 0.74
353 with the mean value equal to 0.54. The values of seismic moment depend mainly on the
354 accuracy in determination of the spectral level by manual picking and uncertainties in the
355 wave velocity (cf. equation 1). As the quality of determination of seismic moment is
356 essentially same for P and S wave, the difference in seismic moment estimation reflects
357 possibly the uncertainty of the velocity model used in our study and can be fully suppressed
358 by decreasing the S wave velocity by 150 m/s. This is much below the assumed uncertainty in
359 S wave velocity (±250 m/s). The change in velocity is supported by the calibration shot data.

360 The corner frequencies calculated from S waves (averaged over SH and SV
361 components) and P waves for clusters C1 and C2 are consistent with f_S/f_P ratios equal to ~1.2.
362 The difference may be an intrinsic source effect as well as the result of inappropriate
363 correction for P or S attenuation. The S wave corner frequency, ranging from 199 Hz to
364 327 Hz, was subsequently used to calculate the source radii. It is well known that calculation
365 of the source radius is model-dependent (e.g. Gibowicz & Kijko, 1994). The resulting source
366 radii ranged from 1.6 to 3.5 m and are affected by the uncertainty of the corner frequency
367 estimation (i.e. variations in attenuation). The uncertainties of the source radius estimation did

368 not exceed 3 m (see Table 1 for details). The relation between seismic moment and source
369 radius and corner frequency is shown in Figure 10, together with uncertainties of seismic
370 moment and corner frequency estimations and the lines of constant static stress drop ranging
371 from 0.01 to 100 MPa. The values of static stress drop range from 0.04 to 1.21 MPa. They
372 are, however, strongly affected by the uncertainty coming from source radius (78% of total
373 error) and seismic moment (22%). As a result, static stress drop can vary by a factor of max.
374 6.7.

375 The calculated energy estimates generally provide an intermediate energy release
376 values comparable to other studies within the same magnitude range, with values ranging
377 from 0.9 to 449 J. Interestingly, cluster C2 present the lowest values of radiated energy and
378 this also applies to seismic moment or static stress drop estimates.

379 The uncertainty of apparent stress estimation is directly related to radiated energy
380 (73% of total uncertainty originates from radiated energy). The other source of uncertainty is
381 the seismic moment estimation (24% of the total error). As a result, the values of apparent
382 stress are biased by a factor of 3.2. The values of apparent stress range from 0.01 MPa to
383 0.26 MPa.

384 8. Discussion and Conclusions

385 The level of seismicity observed at the Groß Schönebeck Geothermal site in the North
386 German Basin is very low. The massive fluid injection into volcanic and sandstone formations
387 at >4km depth in the sedimentary basin triggers induced microseismicity at magnitude levels -
388 $1.8 < M_W < -1.0$. The seismic signals do not penetrate thick sediments likely due to the high
389 source-receiver distances, high frequency content of recorded waveforms and attenuation in
390 the evaporite sequence above the reservoir. The seismicity rate is unexpectedly low

391 considering the high injection rates of up to 9 m^3/min and maxmum injection pressures of
392 nearly 60 MPa at the well-head. This is in contrast to induced seismicity observed in granitic
393 environment, e.g. at Soultz-sous-Forêts / France and KTB / Germany. There, thousands of
394 seismic events were recorded (with significantly larger event magnitudes) during injection
395 experiments at much lower injection rates and well-head pressure, but with similar source-
396 receiver geometries. This cannot be explained by the substantially higher noise level during
397 injection as no major increase of the seismicity rate was observed during injection phases with
398 low surrounding noise. It is obvious that the local geologic and tectonic settings are causing
399 the difference in seismicity rate, and that comparable pore-pressure perturbations generated
400 during fluid injection are not the only criterion to cause brittle failure during rock fracturing.
401 The volcanic rocks at the Groß Schönebeck site might provide only limited shear strength
402 accumulated on existing fractures compared to crystalline rock environments in Soultz or at
403 the KTB. The fact that only two individual microseismic events were induced during the
404 sandstone stimulation may be attributed to the possible different travel paths of fluids, which
405 were injected directly into sandstone deposits, characterized by even more limited shear
406 strength compared to the volcanics (Moeck et al., 2009).

407 Besides of the low seismicity rate during the stimulation phase, the activity stopped
408 after the stimulation episodes and shut-in of the well (clusters B and C). This confirms
409 findings from other injection tests independent of the local rock formation indicating that
410 especially larger (and thus easier detectable) events seem to occur predominantly after
411 injection phases, related to a sudden drop in injection rate and well-head pressure. It is still
412 not clear however, why the events have not occurred after the earlier episodes of high-
413 injection rate followed by the drop down in injection rate and well-head pressure, e.g. on
414 August 12th and 13th, as the injection and pressure history were similar to the later episodes

415 with recorded seismicity.

416 The majority of analyzed events form a plane structure striking ~17º and dipping ~52º
417 ESE. Despite of uncertainties in the location accuracy described earlier, the orientation of the
418 planar structure seems to be in very good agreement with the recent findings of Moeck et al.
419 (2008, 2009), where the highly shear-stressed minor fault system located in the vicinity of
420 injection wells is striking and dipping in the similar direction. Also, the waveforms from
421 clusters B and C1 represent a significant degree of similarity as determined from cross-
422 correlation analysis, suggesting a similar focal mechanism. As a conclusion, the spatial
423 distribution of events in comparison to their source radii not exceeding 3.5±3.0 m may
424 indicate repeated slip on individual patches. Such behavior was observed in a number of data
425 sets of induced seismicity (e.g. Baisch and Harjes, 2003) as well as from natural
426 microseismicity, e.g. at the Parkfield segment of the San Andreas Fault in central California
427 (Waldhauser et al., 2004). Moreover, we observe the migration of events outward from the
428 injection area. Therefore we think that almost all events considered in this paper (clusters B
429 and C1) are attributed to the reactivation of fault plane(s) due to the increased pore pressure in
430 the vicinity of the injection point.

431 We found seismic moment release with moment magnitudes extending over -
432 $1.8 < M_W < -1.0$ and source radii not exceeding 3.5±3.0 m. Seismic moments of the events are
433 relatively smaller than events analyzed in other studies in the same frequency range
434 (Gibowicz et al., 1991; Urbancic & Young, 1993; Urbancic & Trifu, 1996, Oye et al., 2005)
435 (cf. Figure 10). This cannot be explained by the uncertainties coming from velocity model,
436 radiation pattern, attenuation or spectral level picking accuracy. The total effect of the
437 aforementioned factors on the seismic moment is shown in Figure 10 as error bars. The
438 calculated values of seismic moment are situated at a lower part of the static stress drop

interval with static stress drop smaller then 1.21 MPa, similar to data from Strathcona mine and Underground Research Laboratory in Canada. These values of static stress drop, even if we consider all the uncertainties, suggest a partial stress drop environment (i.e. not a uniform and coherent release of stress over the fault plane) and complex source processes (e.g. Gibowicz & Kijko, 1994).

Unfortunately, both energy-related estimates (total radiated energy and apparent stress) are strongly affected by assumptions on attenuation factors. The estimations also suffer from theoretical assumption on radiated energy coming from the finiteness of the frequency band and persistent pumping noise (the effect has not been taken into account). However, one may compare the ratio between radiated energy from P and S waves which is better constrained. The high amount of energy released as S wave in comparison to P wave energy suggests dominantly shear-type events. This again supports the idea that the faulting process favors the slip over the (pre-existing?) fault planes rather than the opening of the cracks due to the increase of the pore pressure in which case the amount of energy released as P waves should be larger.

The estimated apparent stress is comparable to other studies and appear to be dependent on seismic moment. In agreement with other studies (e.g. McGarr, 1999; Ide & Beroza, 2001), the scaling relationship between seismic moment and apparent stress is not seen when all individually scaled data sets are compared over a broad magnitude range. It is possible that the dependence may be related either to the different source processes or differences in travel path/attenuation between events from clusters B/C1 and C2. However, the most likely scenario is that we were simply unable to efficiently record and analyze events with higher corner frequencies (thus higher energies) within the same seismic moment range (Ide & Beroza, 2001), what would make the scaling between apparent stress and seismic

463 moment less significant or even not visible. Finally, the average value of the Savage-Wood
464 efficiency (the ratio between apparent stress and static stress drop) for analyzed events is
465 ~0.25. This indicates friction-dominated events, according to nomenclature provided by
466 Richardson and Jordan (2002). These events are similar to tectonic earthquakes and occur on
467 pre-existing planar zones of weakness, such as bedding planes, dikes, and reactivated faults.
468 This is again in agreement with the idea for the mechanism of induced microseismicity
469 recorded in Groß Schönebeck.

470 References

471 Albright J.N., and Pearson, C.F., 1982. Acoustic Emissions as a Tool for Hydraulic Fracture
472 Location: Experience at the Fenton Hill Hot Dry Rock Site. SPE Journal 22(4), pp. 523-530.

473 Andrews, D., 1986. Objective determination of source parameters and similarity of
474 earthquakes of different size, In: Das, S.; Boatwright, J. & Scholz, C. (eds.) Earthquake
475 Source Mechanics 37, pp. 259-267.

476 Baisch, S., and Harjes, H.-P., 2003. A model for fluid-injection-induced seismicity at the
477 KTB, Germany, Bull. Seismol. Soc. Am. 152 (1), pp. 160–170.

478 Baisch, S., Bohnhoff, M., Ceranna, L., Tu, Y., and Harjes, H.-P., 2002. Probing the crust to
479 9 km depth: Fluid injection experiments and induced seismicity at the KTB superdeep drilling
480 hole, Germany, Bull. Seismol. Soc. Am. 92 (6), pp. 2369–2380.

481 Boatwright, J., and Fletcher, J., 1984. The partition of radiated energy between P and S
482 waves, Bull. Seismol. Soc. Am. 71, pp. 361–376.

483 Bohnhoff, M., Baisch, S., and Harjes, H.-P., 2004. Fault mechanisms of induced seismicity at
484 the superdeep German Continental Deep Drilling Program (KTB) borehole and their relation

485 to fault structure and stress field, J. Geophys. Res. 109 pp. B02309.

486 Boore, D., and Boatwright, J., 1984. Average body-wave correction coefficients, Bull.
487 Seismol. Soc. Am. 74, pp. 1615–1621.

488 Bourouis, S., and Bernard, P., 2007. Evidence for coupled seismic and aseismic fault slip
489 during water injection in the geothermal site of Soultz (France), and implications for
490 seismogenic transients, Geophys. J. Int. 169, 723–732.

491 Brune, J.N., 1970. Tectonic stress and spectra of seismic shear waves from earthquakes,
492 J. Geophys. Res. 78, pp. 4997–5009.

493 Brune, J.N., 1971. Correction, J. Geophys. Res. 76, 5002.

494 Charléty, J., Cuenot, N., Dorbath, C., Dorbath, L., Haessler, H., and Frogneux, M., 2007.
495 Large earthquakes during hydraulic stimulations at the geothermal site of Soultz-sous-Forêts,
496 Int. J. Rock Mech. Min. Sci. 44, pp. 1091–1105.

497 Cuenot, N., and Charléty, J., Dorbath, L., and Haessler, H. , 2006. Faulting mechanisms and
498 stress regime at the European HDR site of Soultz-sous-Forêts, France, Geothermics 35,
499 pp. 561–575.

500 Darnet, M., Marquis, G., and Sailhac, P., 2006. Hydraulic stimulation of geothermal
501 reservoirs: fluid flow, electric potential and microseismicity relationships, Geophys. J. Int.
502 166, pp. 438–444.

503 Di Bona, M., and Rovelli, A., 1988. Effects of the bandwidth limitation on stress drops
504 estimated from integrals of the ground motion, Bull. Seismol. Soc. Am. 78, pp. 1818-1825.

505 Evans, K.F., Moriya, H., Niitsuma, H., Jones, R.H., Phillips, W.S., Genter, A., Sausse, J.,

506 Jung, R., and Baria, R., 2005. Microseismicity and permeability enhancement of
507 hydrogeologic structures during massive fluid injections into granite at 3 km depth at the
508 Soultz HDR site, Geophys. J. Int. 160, pp. 388-412.

509 Gibowicz, S.J., and Kijko, A., 1994. An introduction to mining seismology, San Diego,
510 Academic Press.

511 Gibowicz, S.J., Young, R.P.,Talebi, S., and Rawlence, D. J., 1991. Source parameters of
512 seismic events at the Underground Research Laboratory in Manitoba, Canada: Scaling
513 relations for events with moment magnitude smaller than 2, Bull. Seism. Soc. Am. 81,
514 pp. 1157-1182.

515 Hanks, T.C., and Kanamori, H., 1979. A moment magnitude scale, J. Geophys. Res. 84,
516 pp. 2348–2350.

517 Hartzell, S.H., 1978. Earthquake aftershocks as Green's functions, Geophys. Res. Lett. 5,
518 pp. 1-5.

519 Ide, S., and Beroza, G.C., 2001. Does apparent stress vary with earthquake size? Geophys.
520 Res. Lett. 28 (17), pp. 3349-3352.

521 Jahr, T., G. Jentzsch, A. Gebauer, and T. Lau, 2008. Deformation, seismicity, and fluids:
522 Results of the 2004/2005 water injection experiment at the KTB/Germany, J. Geophys. Res.,
523 113, B11410, doi:10.1029/2008JB005610.

524 Jost, M.L., Busselberg, T., Jost, O., and Harjes, H.-P., 1998. Source parameters of injection-
525 induced microearthquakes at the KTB deep drilling site, Germany, Bull. Seismol. Soc. Am.
526 88, pp. 815–832.

527 Kovach, R.L., 1974. Source mechanisms for Wilmington oil field, California, subsidence
528 earthquakes. Bull. Seismol. Soc. Am. 64, pp. 699-711.

529 Kümpel, H.-J., Erzinger, J., and Shapiro, A., 2006. Two Massive Hydraulic Tests Completed
530 in Deep KTB Pilot Hole, Scientific Drilling 3.

531 Leonard, M., and Kennett, B.L.N., 1999. Multi-component autoregressive techniques for the
532 analysis of seismograms, Phys. Earth Planet. Interiors 113, pp. 247–264.

533 Madariaga, R., 1976. Dynamics of an axpanding circular fault, Bull. Seismol. Soc. Am. 66,
534 pp. 639–666.

535 McGarr, A, 1991. On a possible connection between three major earthquakes in California
536 and oil production, Bull. Seismol. Soc. Am. 81, pp. 948-970.

537 McGarr, A., 1999. On relating apparent stress to the stress causing earthquake fault slip,
538 J. Geophys. Res. 104, pp. 3003-3011.

539 Moeck, I., Backers, T., and Schandelmeier, H., 2007. Assessment of mechanical wellbore
540 assessment by numerical analysis of fracture growth. EAGE 69th Conference and Exhibition,
541 445 11-14 June 2007, extended abstracts volume, D047, London, UK.

542 Moeck, I., Schandelmeier, H., and Holl, H.-G., 2008. The stress regime in a Rotliegend
543 reservoir of the Northeast German Basin, Int. J. Earth Sci., doi: 10.1007/s00531-008-0316-1.

544 Moeck, I., Kwiatek, G., and Zimmermann, G., 2009. Slip tendency analysis, fault reactivation
545 potential and induced seismicity in a deep geothermal reservoir, J. of Struct.Geol., doi:
546 10.1016/j.jsg.2009.06.012

547 Mueller, C.S., 1985. Source pulse enhancement by deconvolution of an empirical Green's

548 function, Geophys. Res. Lett. 12, pp. 33-36.

549 Nagano, K., Moriya, H., Asanuma, H., Sato, M., Niitsuma, H., and Kaieda, H., 1994.
550 Downhole AE measurement of hydraulic fracturing in Ogachi HDR model field, J. Geotherm.
551 Res. Soc. Japan 16, pp. 85-108.

552 Oye, V., Bungum, H., and Roth, M., 2005. Source parameters and scaling relations for
553 mining-related seismicity within the Pyhäsalmi ore mine, Finland, Bull. Seismol. Soc. Am. 95
554 (3), pp. 1011–1026.

555 Phillips W.S., Fairbanks T.D., Rutledge J.T., and Anderson, D.W., 1998. Induced
556 microearthquake patterns and oil-producing fracture systems in the Austin chalk.
557 Tectonophysics doi: 10.1016/S0040-1951(97)00313-2.

558 Phillips, W.S., Rutledge, J.T., House, L.S., and Fehler, M.M.C., 2002. Induced
559 Microearthquake Patterns in Hydrocarbon and Geothermal Reservoirs: Six Case Studies. Pure
560 and Appl. Geophys. 159, pp. 345-369.

561 Plesĭnger, A., Hellweg, M., and Seidl, D., 1986. Interactive high-resolution polarization
562 analysis of broadband seismograms, J. Geophys. 59, pp. 129–139.

563 Raleigh, C.B., Healy, J.H. and Bredehoeft, J.D., 1972. Faulting and crustal stress at Rangely,
564 Colorado. Flow and Fracture of rocks, American Geophysical Union Geophysical Monograph
565 16, pp. 275-284.

566 Richardson, E., and Jordan, T., 2002. Seismicity in deep gold mines of South Africa:
567 Implications for tectonic earthquakes, Bull. Seismol. Soc. Am. 92, pp. 1766–1782.

568 Shapiro, S. A., J. Kummerow, C. Dinske, G. Asch, E. Rothert, J. Erzinger, H.-J. Kümpel, and

569 R. Kind, 2006. Fluid induced seismicity guided by a continental fault: Injection experiment of
570 2004/2005 at the German Deep Drilling Site (KTB), Geophys. Res. Lett., 33, L01309,
571 doi:10.1029/2005GL024659.

572 Simiyu, S.M., 1999. Induced micro-seismicity during well discharge: OW-719, Olkaria,
573 Kenya rift; Geothermics 28, pp. 785-802.

574 Snoke, J.A., 1987. Stable determination of (Brune) stress drop, Bull. Seism. Soc. Am. 77,
575 pp. 530-538.

576 Tosha, T., Sugihara, M., and Nishi, Y., 1998. Revised hypocenter solutions for
577 microearthquakes in the Kakkonda geothermal field, Japan, Geothermics 16, pp. 442-460.

578 Trautwein, U., and Huenges, E., 2005. Poroelastic behaviour of physical properties in
579 Rotliegend sandstones under uniaxial strain, Int. J. Rock Mech. Min. Sci. 42, pp. 924-932.

580 Urbancic, T.I., and Young, R.P., 1993. Space-time variations in source parameters of mining-
581 induced seismic events with $M < 0$, Bull. Seismol. Soc. Am. 83, pp. 378–397.

582 Urbancic, T.I., and Trifu, C.-I., 1996. Effects of rupture complexity and stress regime on
583 scaling relations of induced microseismic events, Pure Appl. Geophys. 147, pp. 319-343.

584 Waldhauser, F., Ellsworth, W.L., Schaff, D.P., and Cole, A., 2004. Streaks, multiplets, and
585 holes: High-resolution spatio-temporal behavior of Parkfield seismicity. Geophys. Res. Lett.
586 31, pp. LI18608, doi: 10.1029/2004GL020649.

587 Weber, M., Zetsche, F., Ryberg, T., Schulze, A., Spangenberg, E., and Huenges, E., 2005.
588 Seismic detection limits of small, man-made reflectors: A test at a geothermal site in Northern
589 Germany, Bull. Seismol. Soc. Am. 95, pp. 1567-1573.

590 Yokota, T., Zhou, S., Mizoue, M., and Nakamura, I., 1981. An automatic measurement of
591 arrival time of seismic waves and its application to an on-line processing system, Bull.
592 Earthquake Res. Inst. Univ. Tokyo 55, pp. 449-484.

593 Zimmermann, G., Reinicke, A., Brandt, W., Blöcher, G., Milsch, H., Holl, H.-G., Moeck, I.,
594 Schulte, T., Saadat, A., and Huenges, E., 2008. Results of stimulation treatments at the
595 geothermal research wells in Groß Schönebeck/Germany, Proceedings of the Thirty-Third
596 Workshop on Geothermal Reservoir Engineering, Stanford University, Stanford, California,
597 January 28-30, SGP-TR-185.

598 Zimmermann,G., Moeck, I., Blöcher, G., 2009a. Cyclic waterfrac stimulation to develop an
599 enhanced geothermal system (EGS) – Conceptual design and experimental results,
600 Geothermics, doi:10.1016/j.geothermics.2009.10.003.

601 Zimmermann, G., Tischner, T., Legarth, B., and Huenges, E., 2009b. Pressure-dependent
602 Production Efficiency of an Enhanced Geothermal System (EGS): Stimulation Results and
603 Implications for Hydraulic Fracture Treatments , Pure and Appl. Geophys. 166 (5-7), pp.
604 1089-1106.

605 Zimmermann, G., Reinicke, A., 2010. Hydraulic stimulation of a deep sandstone reservoir to
606 develop an Enhanced Geothermal System: Laboratory and field experiments. Geothermics,
607 doi:10.1016/j.geothermics.2009.12.003.

608 Zoback, M., Harjes, H.-P., 1997. Injection induced earthquakes and the crustal stress at 9 km
609 depth at the KTB deep drilling site, Germany, J. Geophys. Res. 102, pp. 18477-18492.

610

611 Figure captions

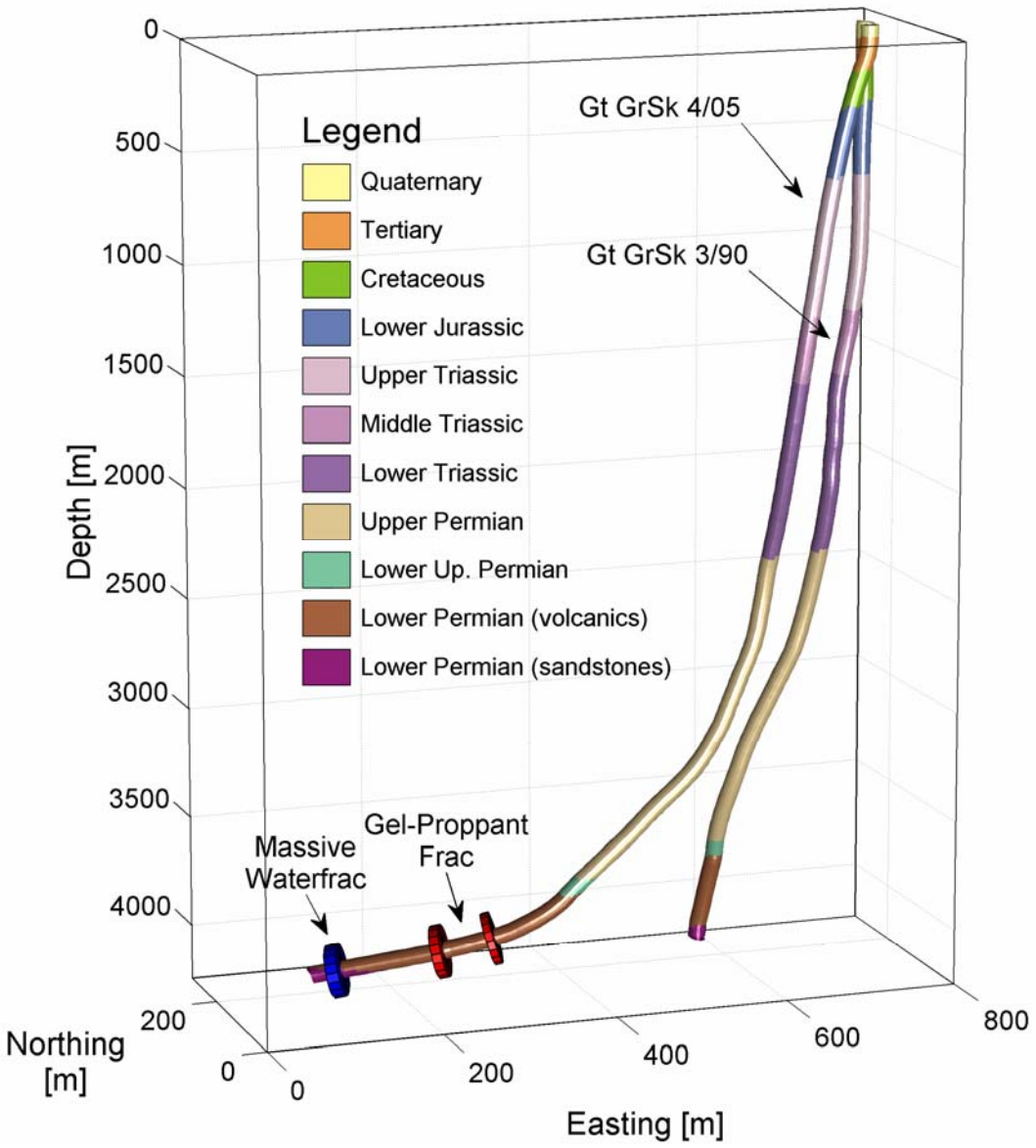

612

613 Figure 1: Alignment of the well paths and the fracture treatments of the doublet system at the

614 Groß Schönebeck drill site after Zimmermann et al. (2008).

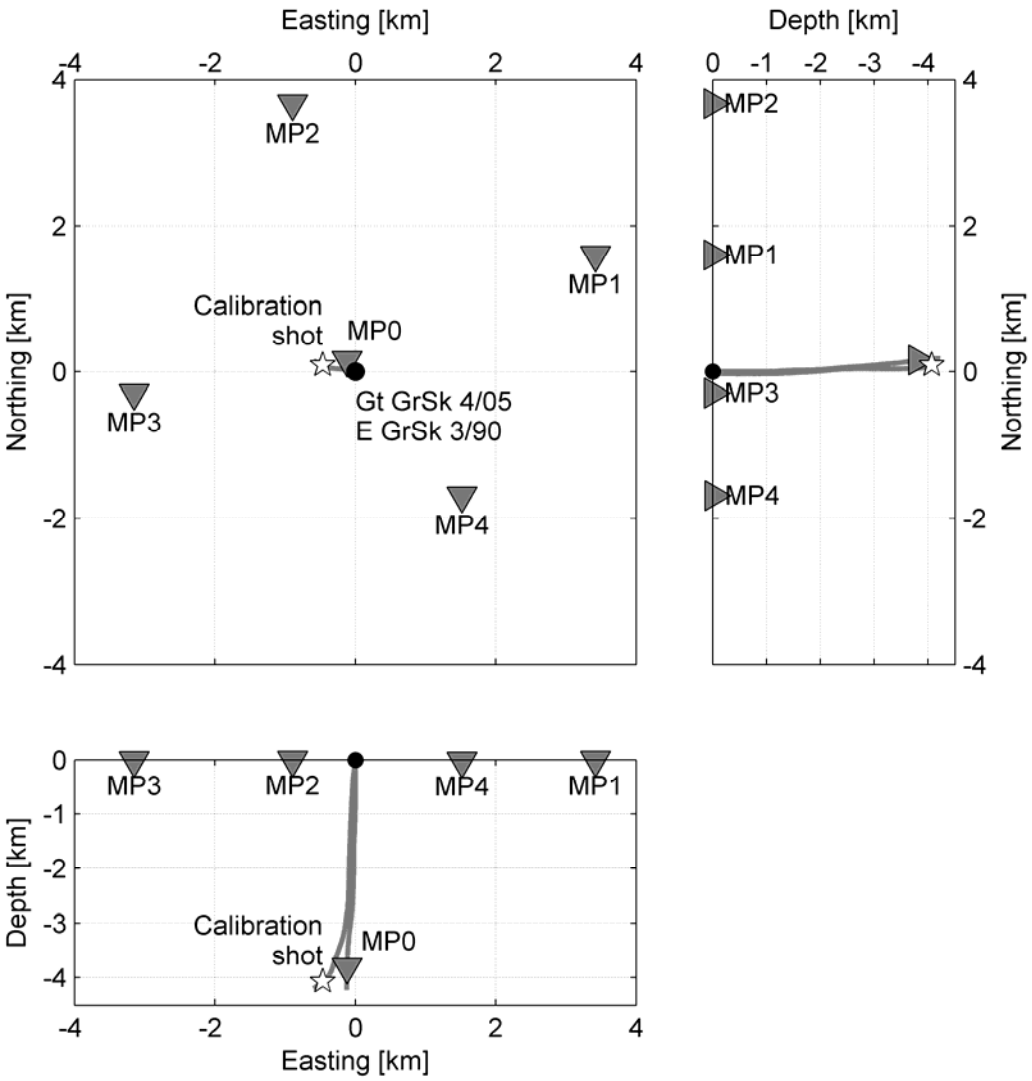

615

616 Figure 2. Temporary seismic network installed at the Groß Schönebeck Geothermal
617 Laboratory during the injection experiment. Seismometer locations are denoted with triangles.
618 The location of the calibration shot is indicated by a star. MP1 and MP3 sites were composed
619 of both surface and shallow borehole stations (60 m depth), MP2 and MP4 sites have only
620 seismometers in shallow boreholes. The black dot is the well head.

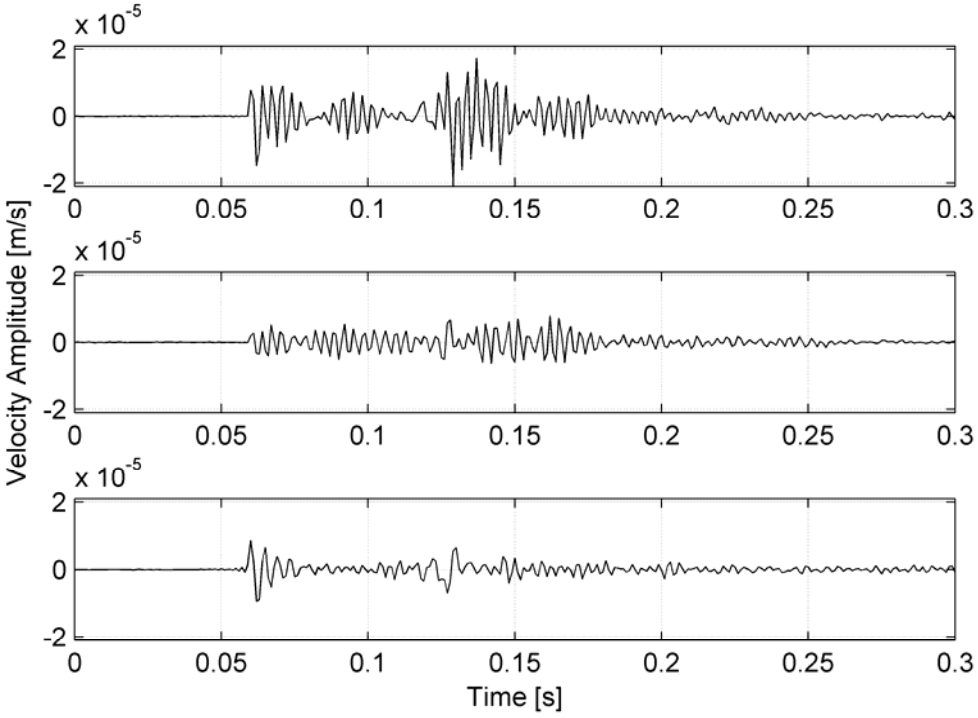

621

622 Figure 3. Sample waveforms of recorded calibration shot (Z, N, E components from top to

623 bottom) fired at ~500 m distance from the deep borehole seismometer.

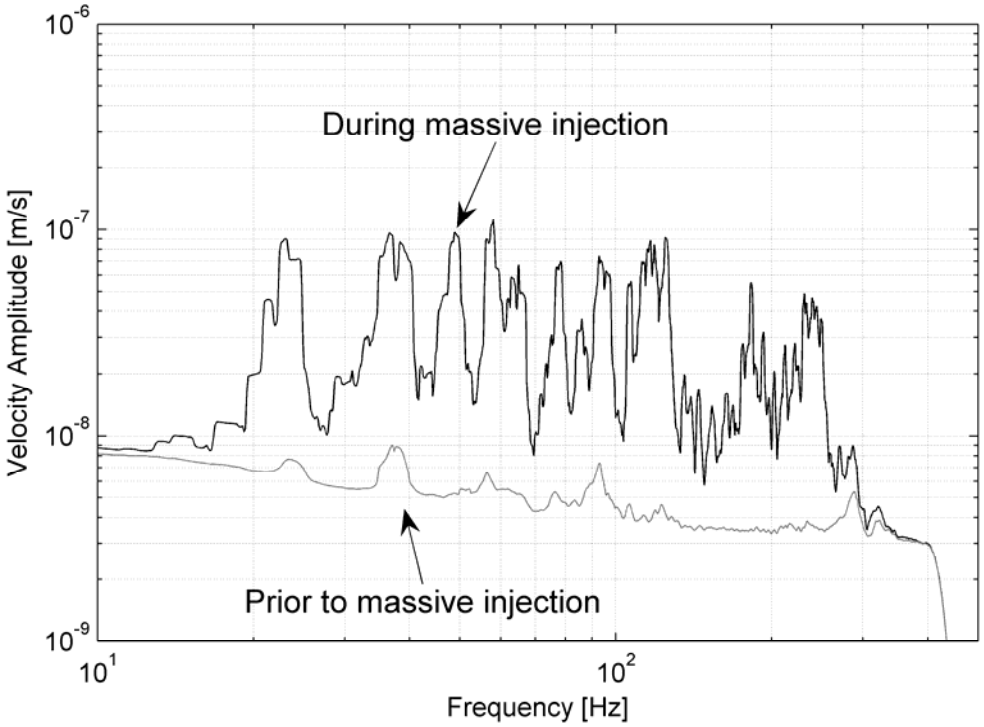

624

625 Figure 4. Average noise levels recorded at the deep borehole seismometer during injection
626 experiments. The black line shows the noise level at high injection rates, grayed - at very low
627 injection rates.

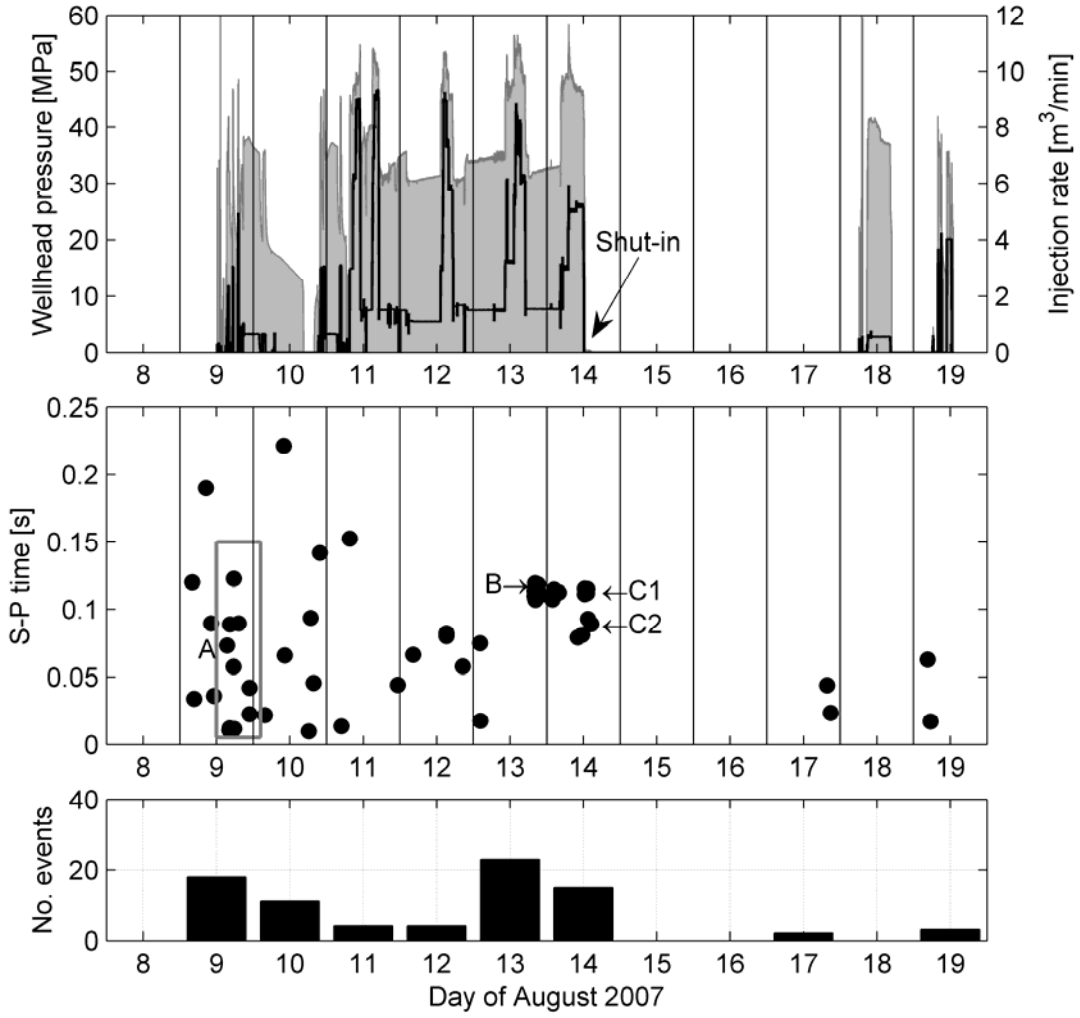

628

629 Figure 5. Top panel: Well-head pressure (shaded area) and injection rate (black line) during
630 the major (Aug 9-14) and the first minor (Aug 18-19) injection experiments. Middle panel: S-
631 P-wave differential travel times of seismic events, detected at the deep borehole sensor. The
632 arrows and rectangle mark the A, B, C1 and C2 clusters analyzed in this study (see Figure 9
633 and Table 1). Bottom panel: Daily rate of detected seismic events.

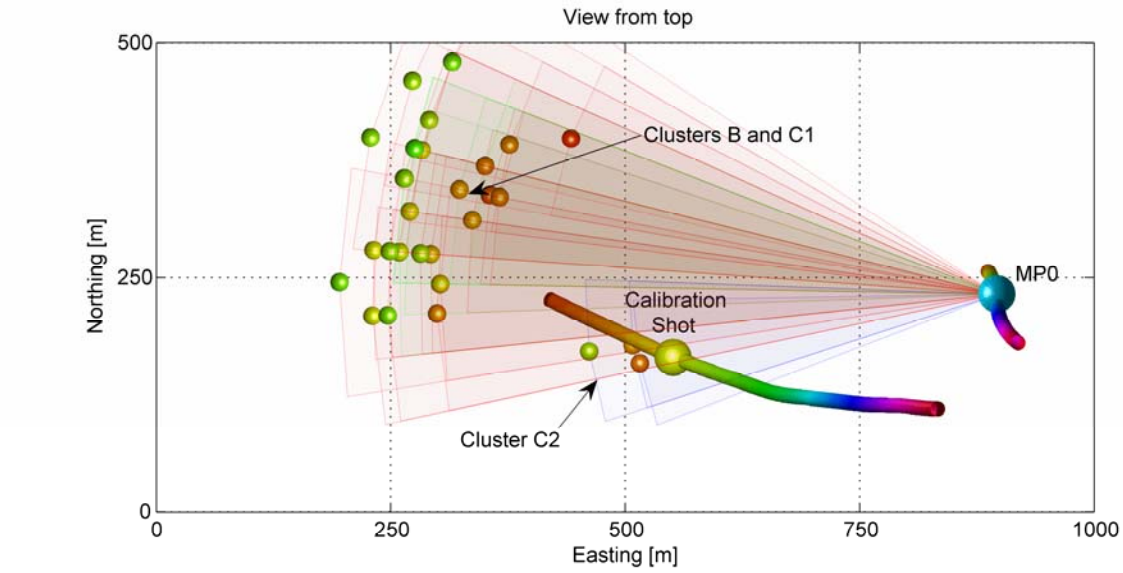
View from top
Clusters B and C1
MP0
Calibration
Shot
Cluster C2
Northing [m]
Easting [m]
500
250
0
0
250
500
750
1000

635

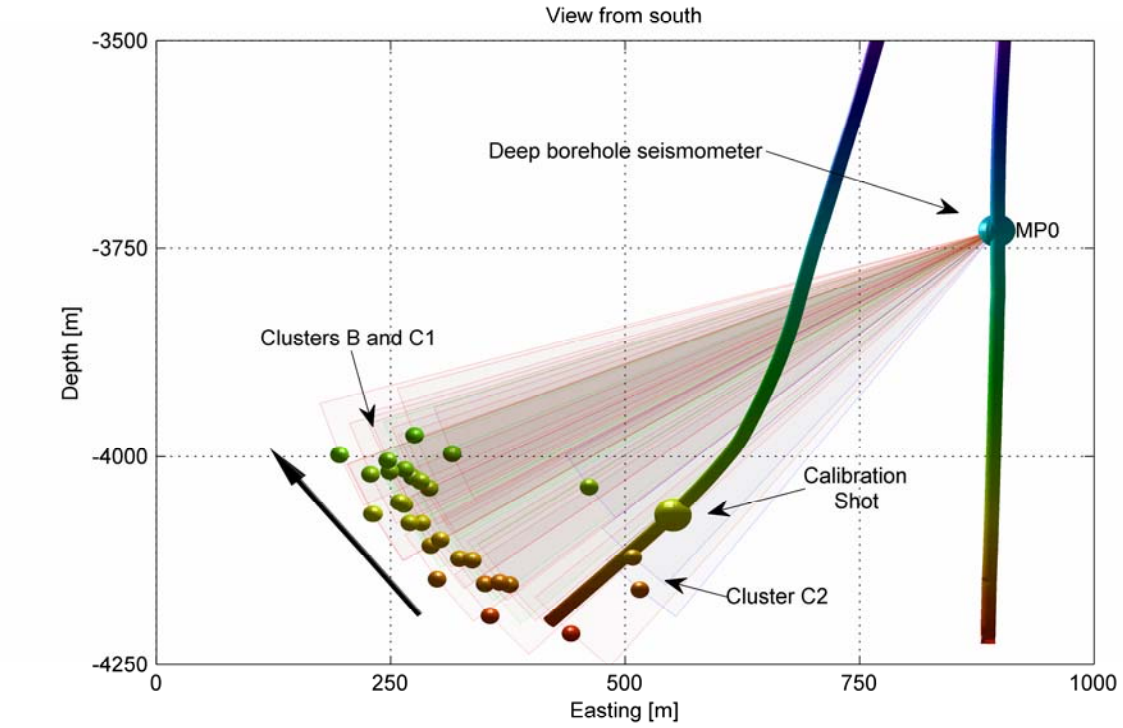
View from south
Deep borehole seismometer
MP0
Clusters B and C1
Calibration
Shot
Cluster C2
Depth [m]
Easting [m]
-3500
-3750
-4000
-4250
0
250
500
750
1000

636

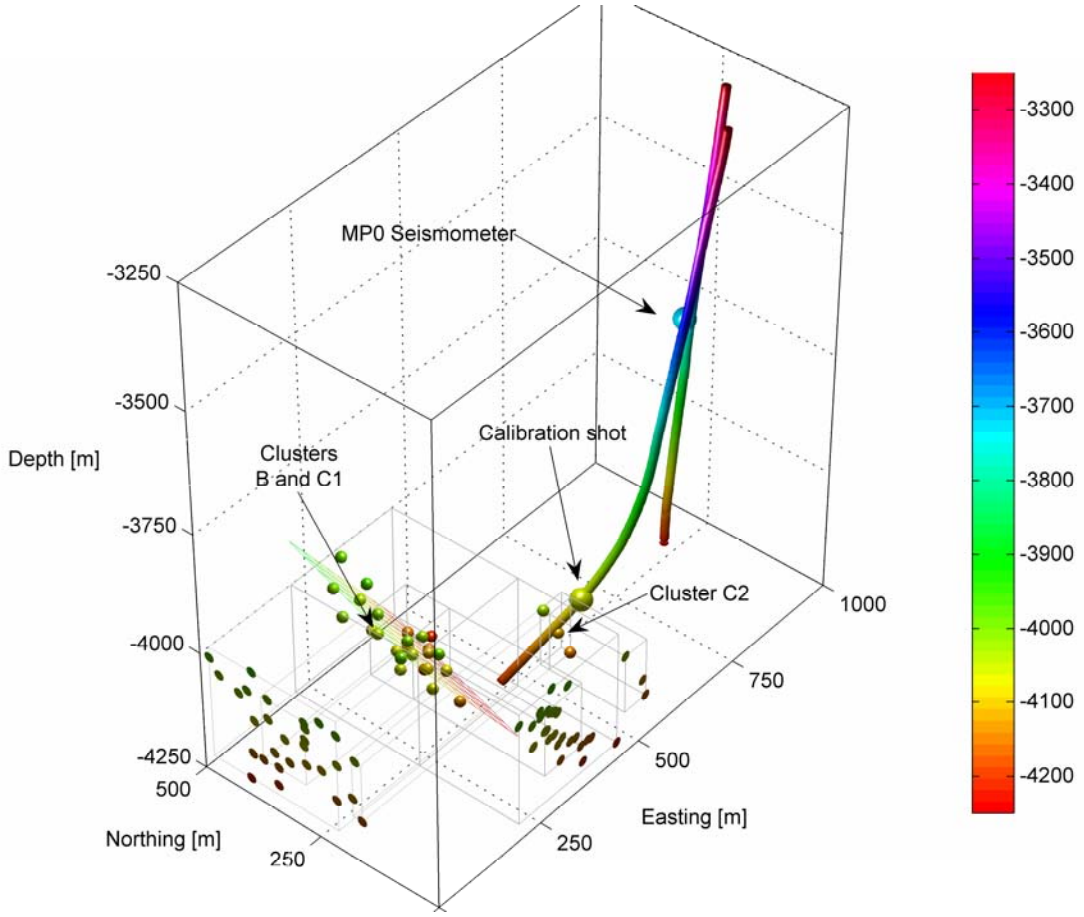

Figure 6. Hypocenter distribution of induced seismic events at the Groß Schönebeck geothermal site as determined from three-component recordings of the deep borehole seismometer. Color reflects the hypocentral depth of events plotted in accordance with the borehole trajectory for comparison. Top (a): Map view of hypocenters. Semi-transparent fans denote maximum horizontal error as discussed in the text. Middle (b): Depth section seen from South. Semi-transparent fans denote maximum vertical error as discussed in the text. The thick black arrow shows the migration of seismic events with time for cluster B and C1. Bottom (c): Perspective view seen from the Southwest: The colored plane reflects the least squares fit to the locations of events from clusters B and C1. The events are also projected to the western and southern side of the bounding box.

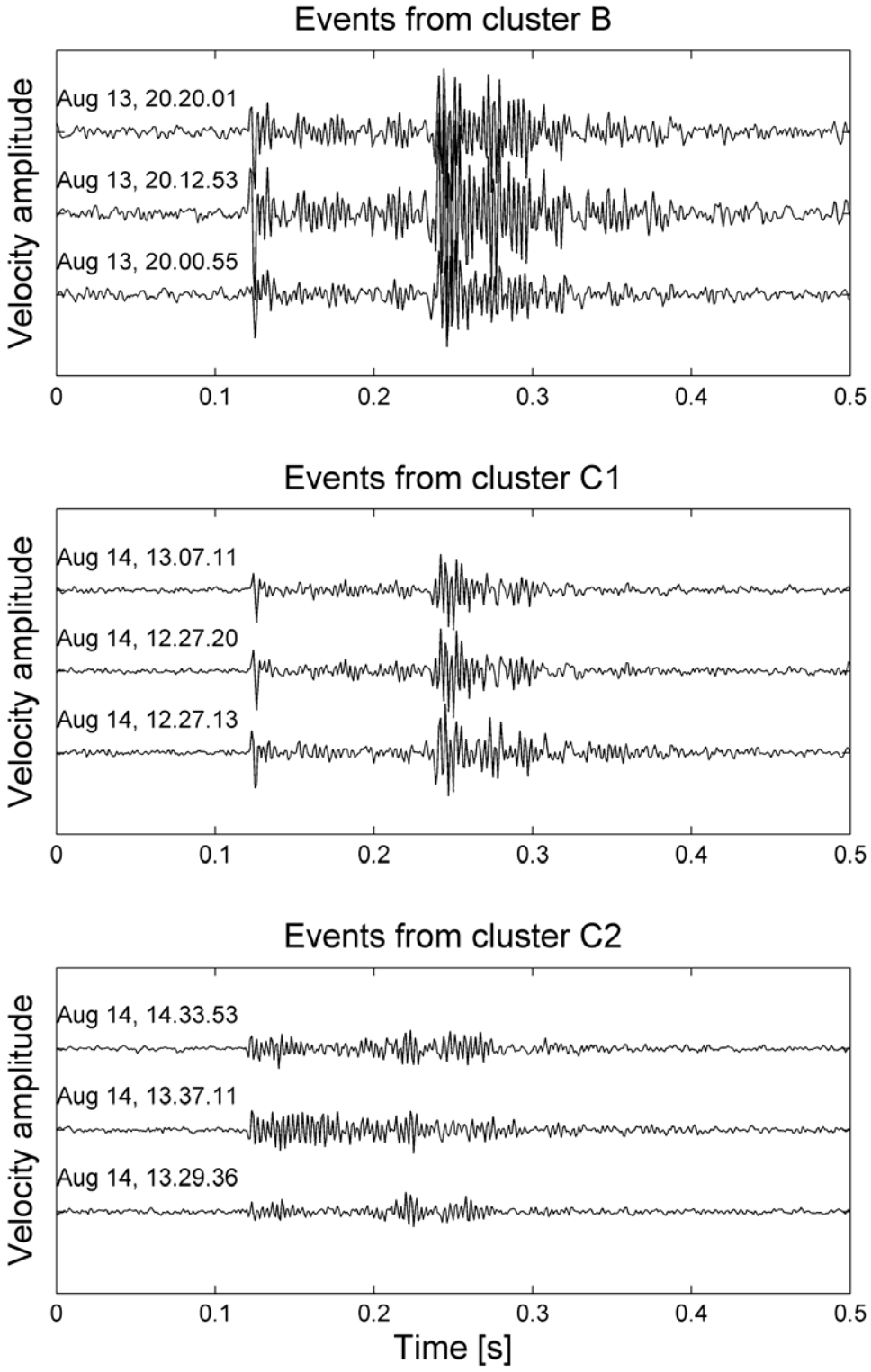

649

650 Figure 7. Examples of waveforms recorded at the downhole sensor during the injection

651 experiment. Each panel presents the vertical component for three recorded events from
652 clusters B, C1 and C2, respectively, from top to bottom. Amplitudes are uniformly scaled.

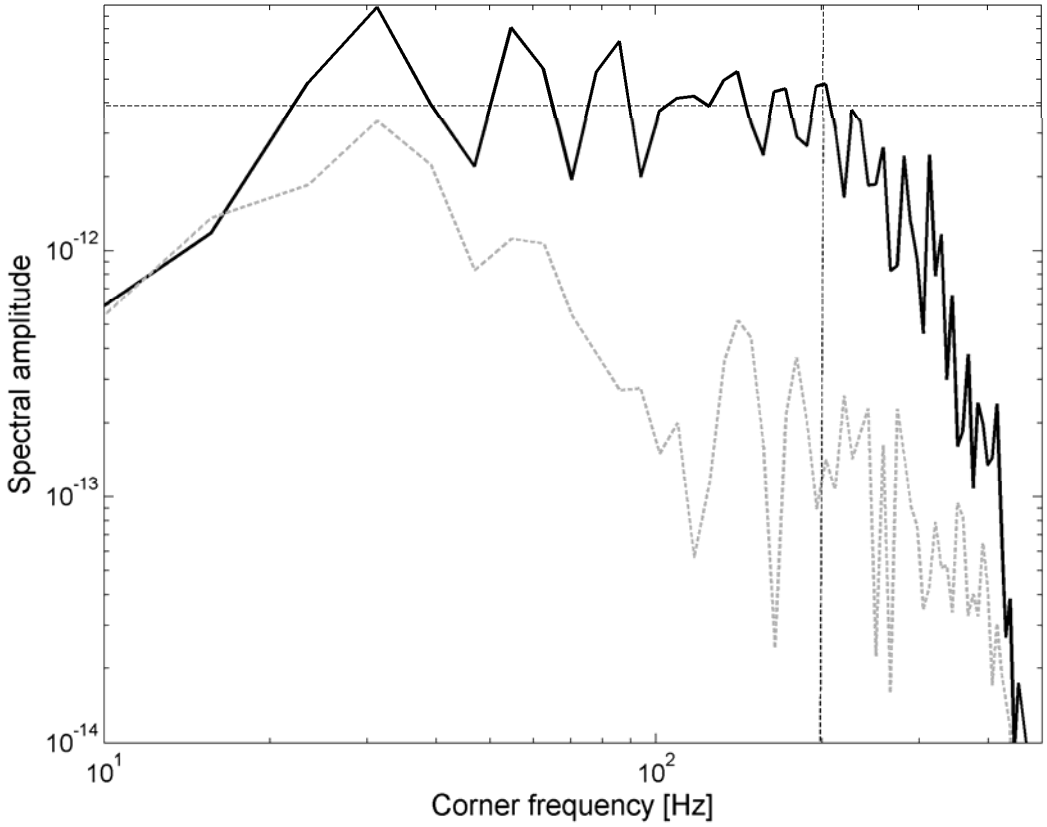

653

654 Figure 8. Example of displacement spectrum calculated from radial component (sequence C1,
655 event 25, see Table 1 for details). The noise level is shown with grayed line. The dashed lines
656 mark spectral level and corner frequency selection.

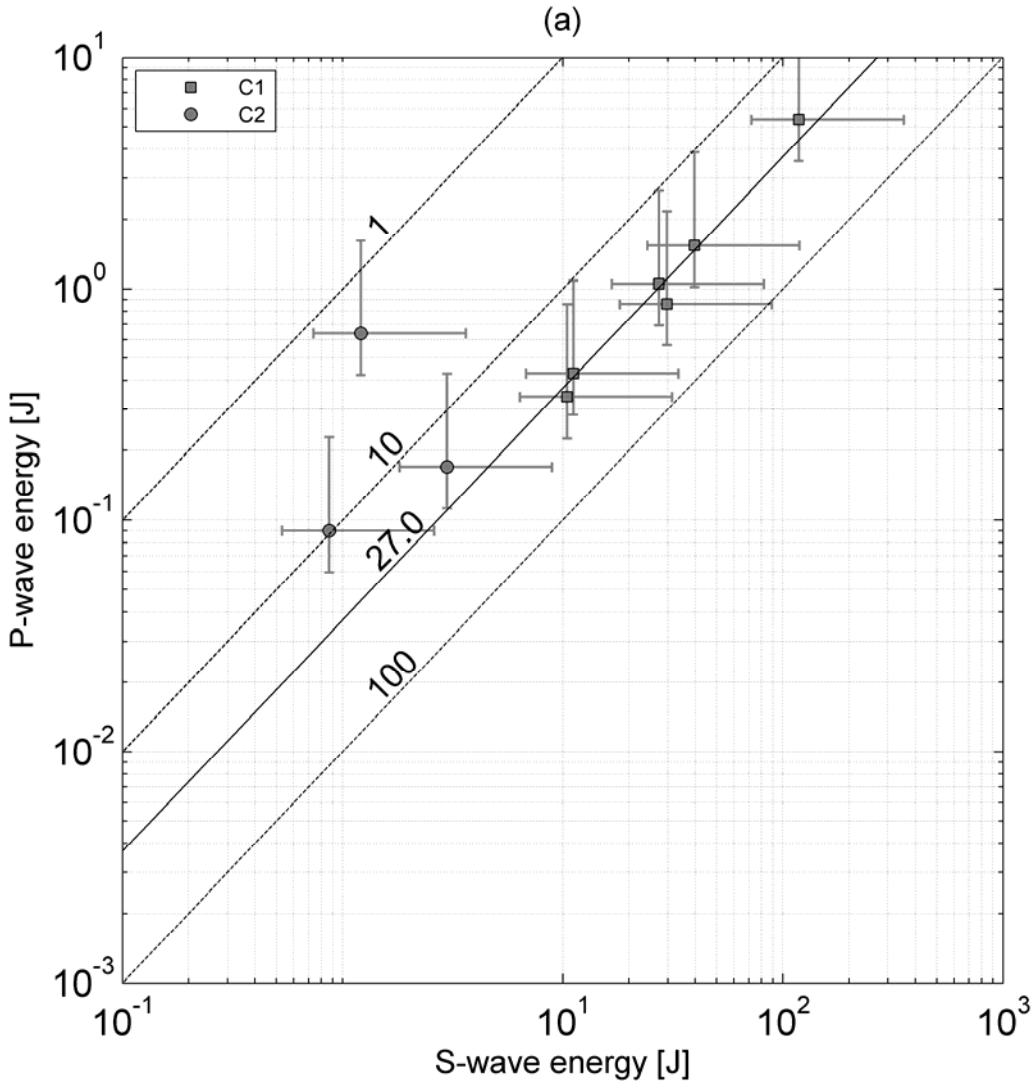
(a)
C1
C2
1
10
27.0
100
P-wave energy [J]
S-wave energy [J]
10^{1}
10^{0}
10^{-1}
10^{-2}
10^{-3}
10^{-1}
10^{1}
10^{2}
10^{3}

658

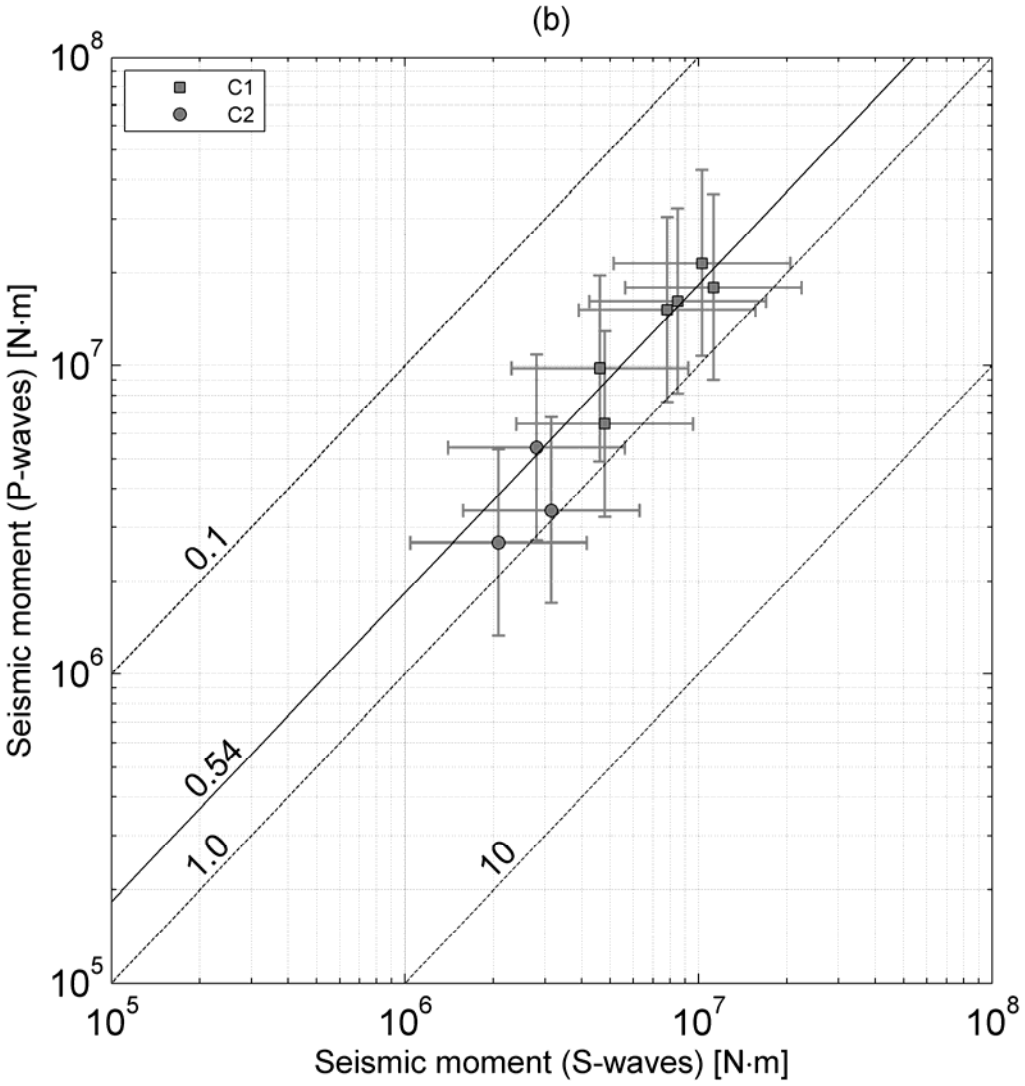

659

660

661 Figure 9. The dependence between (a): energy radiated from S (E_S) and P (E_P) waves and (b):
662 seismic moment calculated from S (M_0^S) and P waves (M_0^P) for events from clusters C1 and
663 C2. The values of constant E_S/E_P and M_0^S/M_0^P equal to 0.1, 1.0 and 10 are also shown. The
664 median value of corresponding ratios for events from cluster C1 is marked with solid line.
665 The error bars shows the uncertainty of radiated energy (a) or seismic moment (b) estimation.

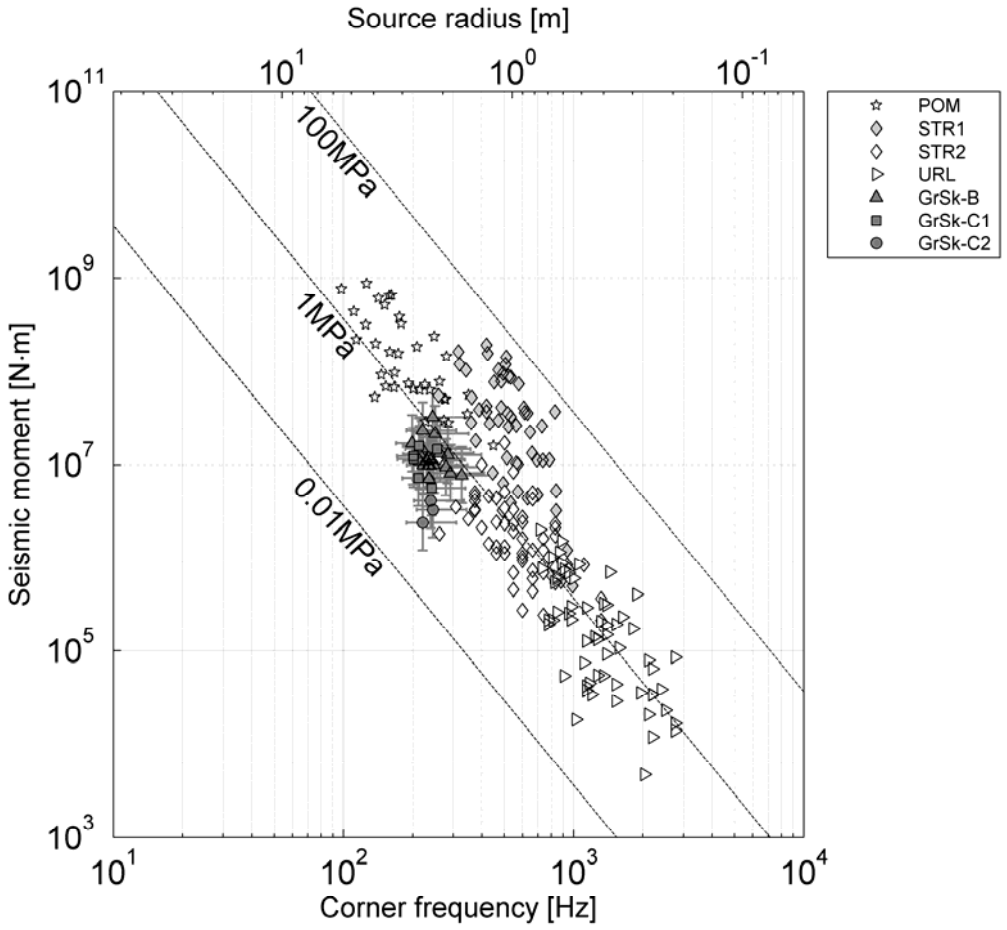

666

667 Figure 10. The dependence between seismic moment and corner frequency and source radius
668 for three analyzed clusters: B (black triangles), C1 (black squares) and C2 (black circles) in
669 comparison with other studies in similar magnitude range: POM (start) – Pyhasalmi ore mine,
670 Finland (Oye et al., 2005), URL (rotated triangles) – Underground Research Laboratory
671 (Gibowicz et al., 1991), STR1, STR2 (light and dark grey rhombs) – Strathcona mine
672 (Urbancic & Young, 1993; Urbancic & Trifu, 1996). The values of constant static stress drop
673 are shown as lines. The error bars show uncertainty of seismic moment and corner frequency
674 estimates (see text for details).

675 Table captions

676 Table 1. Source parameters of analyzed seismic events from clusters B, C1 and C2 (see text

677 for a detailed explanation).

No.	Day of Aug 2008	Hour	Minute	Second	Distance [m]	Moment Magnitude	Corner Frequency [Hz]	Radiated energy [J]	Source radius [m]	Stress Drop [MPa]	Apparent Stress [MPa]
Sequence B											
1	13	19	56	8,4	700	-1,3	234	20,6	3.0±2.2	0,17	0,04
2	13	20	0	56	683	-1,3	214	59,2	2.5±1.8	0,32	0,10
3	13	20	1	37	719	-1,3	222	24,9	2.3±1.7	0,40	0,05
4	13	20	4	14	690	-1,2	263	89,2	2.9±1.8	0,26	0,12
5	13	20	6	40	714	-1,3	284	90,8	1.7±1.0	1,21	0,13
6	13	20	11	5,3	729	-1,4	292	39,6	1.6±1.0	0,87	0,09
7	13	20	11	49	690	-1,3	237	22,0	1.9±1.5	0,65	0,04
8	13	20	12	53	748	-1,0	244	449,2	2.9±2.0	0,60	0,26
9	13	20	14	26	686	-1,3	247	59,3	2.8±1.9	0,21	0,11
10	13	20	15	55	686	-1,1	250	187,5	2.9±1.9	0,40	0,16
11	13	20	20	1,9	710	-1,1	221	166,5	3.4±2.5	0,28	0,13
12	13	20	23	51	686	-1,3	235	32,0	3.1±2.2	0,18	0,05
13	13	20	29	55	706	-1,3	241	26,2	2.9±2.0	0,21	0,04
14	13	20	29	55	704	-1,2	219	49,1	3.2±2.5	0,21	0,06
15	13	20	42	35	723	-1,2	214	29,5	2.2±1.9	0,57	0,04
16	13	20	42	35	726	-1,3	230	30,2	2.1±1.6	0,57	0,05
17	13	20	55	48	751	-1,4	235	11,0	1.9±1.6	0,45	0,03
18	13	20	55	48	748	-1,4	327	102,9	1.8±0.8	0,66	0,24
19	13	21	7	59	748	-1,2	199	28,9	2.2±2.2	0,72	0,03
20	13	21	42	57	686	-1,3	279	50,6	1.8±1.1	0,79	0,10
Sequence C1											
21	14	12	27	13	717	-1,2	255	129,0	2.8±1.8	0,32	0,16
22	14	12	27	20	704	-1,2	213	37,6	3.3±2.6	0,20	0,04
23	14	12	38	11	704	-1,5	242	10,8	2.9±2.0	0,10	0,04
24	14	12	54	32	723	-1,4	212	10,5	3.4±2.7	0,09	0,03
25	14	13	7	11	704	-1,3	201	24,8	3.5±2.9	0,13	0,04
26	14	13	17	36	723	-1,3	202	26,8	3.5±2.9	0,12	0,04
Sequence C2											
27	14	13	29	36	555	-1,8	221	0,9	3.1±2.4	0,04	0,01
28	14	13	37	11	580	-1,6	239	1,8	2.8±2.1	0,08	0,01
29	14	14	33	53	536	-1,7	245	3,2	2.8±2.0	0,07	0,02

678

679